Collecting fog with vertical fibres: Combined laboratory and in-situ study

Adele Moncuquet, Alexander Mitranescu, Olivier C Marchand, Sophie Ramananarivo, Camille Duprat

Collecting fog with vertical fibres: Combined laboratory and in-situ study

Adele Moncuquet[a], Alexander Mitranescu[a], Olivier C. Marchand[a], Sophie Ramananarivo[a], Camille Duprat[a]

[a] *LadHyX, Ecole polytechnique, Department of Mechanics, Institut Polytechnique de Paris, Palaiseau, France*

Abstract

Fog harvesting is an application of aerosol filtration to capture water droplets from fog by using nets, called fog collectors. It is a promising technique for freshwater supply in arid and semi-arid regions. In this study, we investigate the collection efficiency of harp-like fog collectors consisting of vertical fibres. We conduct well-controlled laboratory scale experiments on model fog collectors and develop a predictive theoretical model accounting for the liquid distribution on the fibres and for aerodynamic effects. Without using any adjustable parameter, we obtain a good agreement between our theoretical model and laboratory scale experimental results. Furthermore, we perform collection efficiency measurements on an in-situ pilot scale fog collector, accompanied by a description of the fog's microphysical properties. Comparing the results of our pilot scale and laboratory scale experiments and the theoretical model developed, we propose a method to accurately evaluate the efficiency of our collector, with simultaneous measurements of collected water volume and fog characteristics.

Keywords: fog, fog collection

1. Introduction

Passive fog gauges are commonly used to collect and characterize fog, either for chemical characterization[1], fresh water exploitation[2, 3], collection of industrial fog [4] or fog vegetation interception and redistribution studies [5, 6, 7]. These gauges generally consist in fibrous nets, from the earlier cylindrical arrangements of vertical parallel fibres as designed by the Atmospheric Sciences Research Center [8, 9, 1], cylindrical screens [10], flat woven meshes (so-called *Standard Fog Collector*) [2], or panels with parallel vertical wires [11, 12], to more recent complex 3D textiles [13]. The principle is simple: the water droplets carried by the fog impact and accumulate on the wires of the gauge, and are then drained by gravity to a collecting tank.

These various designs have different collection efficiencies, and thus yields, depending on the characteristics of the fog and the geometry of the collector, as are reported in an abundant literature; see for example [14] for a recent

review. Inter-mesh comparisons are complex to analyze and show unreliable results [11, 15, 13]. The link to meteorological variables is specific to each design and fog conditions, although a relationship can be accurately obtained with the correct method provided enough data is obtained [12]. Many recent studies aim at optimizing the fog collection, e.g. with multiple layers, complex structures or sophisticated surface treatments [13, 16, 17, 18, 19]. However, the quantity of interest in these studies is generally the flow rate of collected water per unit area of the collector Q_c in $Lh^{-1}m^{-2}$, which depends on the incoming fog conditions, and, while being a good quantity to estimate fog water production yield, it can not be used to evaluate the performance of a collector. Only few studies consider the collection efficiency of single fog events [2, 20], and these studies are limited to the *Standard* or *Large* Fog Collector with a double knitted mesh (specifically a Raschel mesh of solidity 35%). Recently, efforts have been made to build models of the collection processes [14], either of the capture mechanisms [21], structure and wetting properties [22] or aerodynamics [23, 24, 25]. Some models have been tested on active collectors, in which the fog is drawn by a fan to impact the wires at a given velocity [26]. However, there are no direct quantitative comparisons between laboratory scale experimental results, in situ measurements of passive wind-driven fog collection and theoretical predictions.

In this study, we aim at measuring and modeling the collection efficiency of parallel wires fog collectors. We perform well-controlled laboratory scale experiments on model fog collectors consisting of arrays of vertical fibres. The laboratory data allow us to develop a predictive theoretical model containing the relevant physical mechanisms that can be used to quantitatively predict the collection efficiency and to design a robust, efficient fog collector. We then obtain efficiency measurements from an in-situ pilot fog collector placed on the meteorological station SIRTA[27] with concomitant measurements of the microphysics properties of the fog. The results of two campaigns (2019-2020 and 2020-2021) are then compared to our laboratory experiments and our model predictions, and we explore the link between the measured efficiencies and the meteorological variables.

2. Fog collection mechanisms

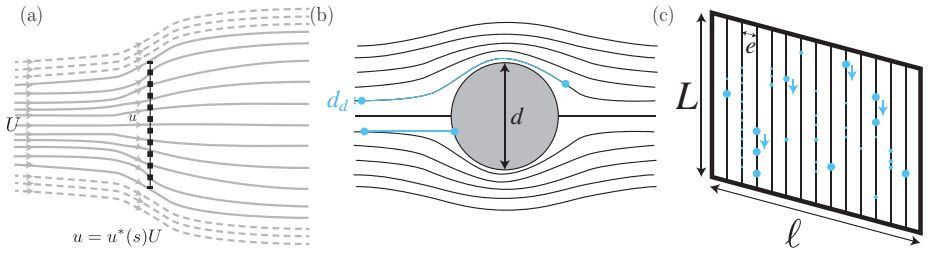

Figure 1: (a) aerodynamic effects. (b) Capture: inertial impact, (c) Coalescences, drainage, re-entrainement.

The principle of passive fog collection is simple: the fog goes through the porous net, the droplets it carries impact the wires of the net to be captured, forming drops on the fibres; these drops merge with incoming droplets, grow, until they eventually fall down due to gravity. The collection efficiency thus depends on these three steps : flow, capture and drainage as shown in Fig. 1 [24, 14, 25]. The net has a solidity s (fraction of solid area over total area, sometimes called "shade coefficient" for textiles, and linked to the porosity $\phi = 1 - s$), and acts as an obstacle for the flow: part of the fog will go through the porous net, while part may be deviated around the net; this is characterized by an aerodynamic efficiency η_a (Fig. 1(a)). Then, only part of the incoming droplets carried by the flow may be captured; this is characterized by a deposition, or capture efficiency η_c [14, 16] (Fig. 1(b)). Finally, the fog droplets merge on the fibres, forming large drops that have to be drained out of the net without being re-entrained by the flow. The amount of drops that may fall down and be collected below the net is characterized by the drainage efficiency η_d (Fig. 1(c)). The overall efficiency may be written as [14, 16]

$$E = \eta_a \eta_c \eta_d. \tag{1}$$

The aerodynamics has two main effects that we will discuss further in the following: the incoming normal velocity in front of the net is reduced to u such that $u = U u^*(s)$, where the velocity reduction $u^*(s)$ depends on the net solidity, and part of the streamlines are deviated around the net (dashed streamlines in Fig. 1(a)). A model of the aerodynamic efficiency was proposed by considering a superposition of the potential flow around a solid obstacle and a free flow through the voids of the net [24] as

$$\eta_a = \frac{s}{1 + \sqrt{\zeta / C_D}}, \tag{2}$$

where ζ is the pressure drop coefficient that depends on the fine structure (e.g. fibres) and C_D is the drag coefficient of the net that depends on its overall shape. A discussion of this model is provided in [14]. When no blockage effects are present, i.e. the flow can move through the net without resistance ($\zeta / C_D \ll 1$), this aerodynamics efficiency reduces to $\eta_a = s$, i.e. takes into account the fact that only the fog reaching the fibres may be captured.

The main mechanism for capture, apart from direct interception, is the inertial impact of droplets [28]. We consider a uniform flow, of velocity U far from the collector, of a fog of density ρ and viscosity μ, carrying liquid droplets (density ρ_d) of diameter d_d. The carrier fluid flows with velocity $\mathbf{u_f}$ around a fibre of diameter d, and the trajectory of a droplet of velocity $\mathbf{u_d}$ is given by

$$\frac{\pi}{6} \rho_d d_d^3 \frac{\mathrm{d}\mathbf{u_d}}{\mathrm{dt}} = 3\pi\mu d_d \left(\mathbf{u_d} - \mathbf{u_f}\right). \tag{3}$$

This equation can be written in dimensionless form, using U as the typical velocity and $\tau = d/U$ as the typical time (i.e. the time to go around the obstacle),

$$\frac{\mathrm{d}\bar{\mathbf{u}}_\mathbf{d}}{\mathrm{dt}} = \frac{1}{St} \left(\bar{\mathbf{u}}_\mathbf{d} - \bar{\mathbf{u}}_\mathbf{f}\right) \tag{4}$$

with a unique parameter, the Stokes number St

$$St = \frac{\rho_d d_d^2 U}{9\mu d} \tag{5}$$

that expresses the balance between the inertia forces of the droplet and the viscous forces of the fluid, i.e. compares the time for a droplet to be slowed down by viscous effects to the time necessary to go around the obstacle. At small St, the viscous forces of the fluid dominate, the droplets are entrained by the flow and are transported around the fibres: the collection efficiency is low. At high St, the inertia forces dominate, the droplets stay on their trajectories, leave the streamlines and impact the fibres: the collection efficiency is high (Fig. 1(b)). Langmuir and Blodgett [29] developed a model based on potential flow to obtain the fluid velocity $\mathbf{u_f}$, solve (6), and express the efficiency of droplet capture η_c as a function of St. Using a differential analyzer, they obtained graphical solutions that they fitted with empirical equations. Their approximate solution, widely used in aerosol filtration and fog capture [28, 14, 16] reads

$$\eta_c = 0 \qquad St < 0.125 \tag{6a}$$

$$\eta_c = 0.466\ (\log_{10}(8St))^2 \qquad 0.125 < St < 1.1 \tag{6b}$$

$$\eta_c = \frac{St}{St + \frac{\pi}{2}} \qquad St > 1.1 \tag{6c}$$

By studying the case of a single superhydrophilic fiber, for which there are no aerodynamics or re-entrainment effects, i.e. $\eta_a = \eta_d = 1$ and the efficiency if directly given by the efficiency of capture $E = \eta_c$, Jiang et al.[30] showed experimentally that the capture efficiency is indeed given by eq. (6) with an excellent agreement.

In our study, we focus on a model system resembling the wire-harp fog gauges [8, 11], by studying a flat net of parallel evenly spaced vertical fibres. The drops are then free to flow down the fibres to be collected, and drainage is thus not a limiting factor. Furthermore, vertical fibre arrays are less prone to clogging than screens [22, 31, 21, 12] and we consider that there are no clogging nor re-entrainements in the flow, i.e. $\eta_d = 1$. In general, the different efficiencies are not independent and may evolve in time. Indeed, the presence of drops accumulated on the net decreases the permeability of the net to wind which increases the deviation of the flow and/or modifies the capture efficiency as it modifies the surface characteristics. These effects actually reduce the performance of screen gauges with respect to harp-like collectors gauges, thus giving poorer description of the fog phenomena with conventional screen gauges [12]. In our ideal system of vertical fibres, we consider that the drops are quickly evacuated by gravitational drainage, and the efficiencies are independent.

In the following, we first consider widely spaced fibres, i.e. low solidity nets for which no aerodynamic effects are expected. Using controlled laboratory experiments, we develop a theoretical model based on our previous results [21] to predict the capture efficiency quantitatively. We further extend to higher

solidity nets for which aerodynamics effects affect the collection efficiency, and include these aerodynamics effects in our model. From these findings, we propose a new design for collecting nets which we test with a large scale pilot net placed on the SIRTA meteorological station in Palaiseau, France [27]. We report efficiency measurements, and use the comparison to laboratory data and to our model to discuss the link with meteorological variables.

3. Laboratory Experiments: towards a universal model for fog collection

3.1. Materials and Methods

The experiments are conducted with a fog wind tunnel that contains a turbulent chamber (1 m length, 0.5 m width and 0.7 m height) in which fog is produced (Fig. 2 (a)). The bottom of the turbulent chamber is covered by a water basin of 10 cm depth in which 30 ultrasonic mist makers are immersed. These fog makers vibrate at ultrasonic frequencies and excite the water surface to emit water droplets that eventually form the fog. We measure the droplet size distribution produced by the ultrasonic fog makers using a fast camera directly above the fog makers, without flow (see Supplementary information). In the wind tunnel, the droplets will coalesce, leading to a different drop distribution with larger sizes. We measure the drop distribution produced by the fog makers and flowed at a wind speed of 2 m/s through a grid and tube using a laser diffraction method (Helos Sympatec). The resulting distribution is shown in figure 3 (a). While larger drops may be present, most of the generated droplets have diameters comprised between 6 and 10 μm; we estimate that the mean droplet diameter of the fog is $d_d \approx 7.8$ μm. Two sets of ventilators are installed in the turbulent chamber: one above the fog makers, blowing towards the bottom of the chamber and generating a large scale turbulent flow of typical Reynolds number 10^8 to ensure a homogeneous, well-mixed fog, and one at the rear end of the chamber to push the fog through the honeycomb structure. The honeycomb structure and the converging duct ensure a laminar and controlled flow at the exit vein of area $S_{wt} = 0.22 \times 0.22$ m^2, with a flow velocity for the empty vein U' ranging from 0.5 to 3 m/s measured at the exit of the wind tunnel, in the center of the vein, using a vane anemometer. The height of liquid in the basin is kept constant using an overflow system, which allows to measure the volume of produced fog. The fog makers produce a constant flow of water of $Q_{wt} = 6.86$ L/h measured over several hours. We define the water flux per unit area as $q = Q_{wt}/S_{wt}$, which for our wind tunnel is $q = 3.94 \times 10^{-5}$ m/s. Since the water flow produced is constant, the fog density varies as the flow velocity changes. We can define the fog liquid water content (LWC, in g/m^3) as $LWC = \rho_d q/U$. As fog is produced, the tunnel and the laboratory room quickly fill up with dense fog, ensuring that the humidity at the exit of the vein is close to 100%, thus preventing any evaporation of the droplets. During the duration of an experiment (a few minutes), the amount of deposited droplets on the walls and honeycomb structure of the tunnel remains small.

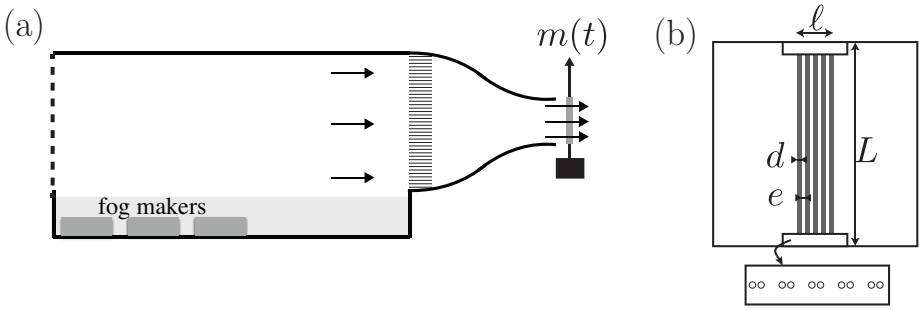

Figure 2: (a) Sketch of the wind tunnel (b) Sketch of a net in the exit vein of the wind tunnel. The fibres are held and positioned with PMMA structures on which a specific pattern is drilled.

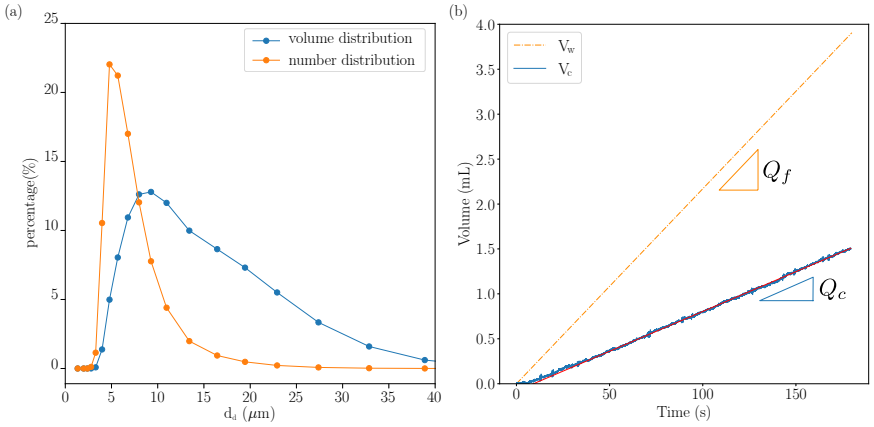

Figure 3: (a) Droplet size distribution d_d of the artificial fog produced by the fog makers, in number (orange) and volume (blue), obtained with laser diffraction. (b) Evolution of the fog water volume passing by the fibres V_{wf} and the volume of water collected V_c with time, for a net of 10 fibres with $d = 250$ μm and $e = 5$ mm.

We install model fog harvesters consisting of a metal frame of $L = 0.22$ m height and $\ell = 0.07$ m width, thus total surface $S_{net} = L\ell$, directly at the exit vein of the fog wind tunnel, keeping a small gap to avoid touching of the collector that would impact weight measurements (Fig. 2 (b)). The collectors are placed at the center of the exit vein and have a small width compared to the tunnel width in order to minimize wall effects and blockage effects. We use a hot wire probe to measure the flow velocity and turbulent intensity at different locations at the exit of the wind tunnel (see Supplementary Information); at the position of the collector, the flow is constant with low turbulent intensity (below 2%). The collectors have PMMA bearing structures at the top and the bottom holding the fibres. We precisely laser-cut holes in these bearing structures to control the spacing and arrangements of the fibres of the nets, adapted to each considered fibre radius. Nylon fibres are threaded through these holes and fixed with crushed aluminum beads to form a tight net of fibres, with a large tension within the fibres. Each net consists of N fibres, with diameters $d = 120 - 600$ μm and thus a projected fibre surface $S_f = NLd$. The spacing between the fibres from $e = 1.8 - 9.6$ mm leads to a large range of solidity $0.074 < s = S_f/S_{net} < 0.34$. As we impose the flow through the ventilators at the back of the turbulent chamber, the presence of the nets causes a pressure drop characterized by the velocity reduction $u^*(s)$ (Fig. 1 (a)), that changes the velocity in the vein. We can estimate the actual flow velocity U as

$$U = U' \left(1 - \frac{\ell(1 - u^*(s))}{L}\right). \tag{7}$$

This reduction is at most $[1 - (\ell/L)] = 68\%$ for a completely solid obstacle (i.e. $s = 1$ and $u^* = 0$), but remains below 8% for the low solidity nets considered here, as we will illustrate in the following. Previous experiments on the same set-up with a reference frame placed at the exit of the wind tunnel indicate that the amount and characteristics of the fog remain constant throughout the experiments, independently of the fog collectors installed in the vein or the day environmental conditions [21].

A basin is attached below the net to collect the water that is drained along the fibres (Fig. 2 (a)). The model nets with the basin are attached to a load cell (LSB200 from Futek[1]) of capacity 20 g that measures the total volume of water collected $V_c(t)$ as a function of time with a 2 mg resolution and an acquisition rate of 200 Hz. When placing a model fog harvester in the fog flow, we can observe that, after a brief transient time, the volume collected V_c increases linearly (figure 3 (b)). The short transient time corresponds to the capture of the first droplets on the dry fibre; the accumulated droplets then merge and start to slide down the fibre. The system quickly reaches a stationary state with a constant collection rate Q_c, given by the slope of $V_c = Q_c t$ (figure 3 (b)).

[1] https://www.futek.com/store/load-cells/s-beam-load-cells/miniature-s-beam-LSB200/FSH03868

We define the quantity of fog that goes through the net as

$$V_w(t) = \int_0^t qS_{net}\mathrm{d}\tilde{t}. \tag{8}$$

Since the fog flow rate is constant, we obtain a linear variation $V_w(t) = Q_w t$ with $Q_w = qS_{net}$. The collection efficiency is thus determined as

$$E = \frac{Q_c}{Q_w} = \frac{Q_c}{qS_{net}}. \tag{9}$$

Here, our nets are an array of vertical parallel fibers, and we can thus describe the net as the sum of individual fibers. We measure the collection of the frame individually and then subtract it from our results in order to obtain the collection rate, and thus the collection efficiency, of the fibres alone. In order to definer this efficiency of the fibers, we need to consider only the volume of liquid encountering the N fibers $V_{wf}(t) = Q_f t$ with $Q_f = qS_f = NqLd$, and not the amount of liquid going through the entire net V_w. The fibers efficiency is thus given by

$$\mathcal{E} = \frac{Q_c}{Q_f} = \frac{E}{s}. \tag{10}$$

We note that this prorosity factor s is generally included in the aerodynamic efficiency η_a; indeed, in the absence of blockage effects, $\eta_a = s$ and $E = \eta_c s$, and indeed $\eta_c = \mathcal{E}$ [14, 16]. Here, we decide to separate the porosity and the aerodynamic effects by considering directly the fibers capture efficiency $\mathcal{E}$, which is the efficiency of the single fibers composing the net.

3.2. Collection surface: liquid morphologies

As a first step, we consider widely spread apart fibres, i.e., low solidity nets ($s < 0.1$), for which no aerodynamic effects are expected ($\eta_a = 1$). All the droplets that are intercepted by the fibres will count for the collection rate (i.e. $\eta_d = 1$). The collection rate of the net is thus simply the sum of the collection rate of individual isolated fibres, and the collection efficiency we will model here is thus directly the fibers capture efficiency $\mathcal{E} = \eta_c$. We thus study a situation identical to the case of a single fiber [30].

As the fog flows across the net of fibres, fog water droplets are intercepted by the fibres, coalesce and form larger drops sitting on the fibres. Above a critical size, these drops fall along the fibres and entrain the drops below them (Figure 4 (a-b)). One way to suppress this drop growth is to use a pair of close fibres (Figure 4 (c), called co-fibres in the following) - indeed, provided the fibres in the pair are closer than a critical distance $\simeq 0.6d$, the liquid will form long liquid columns between the fibres rather than drops [32, 21, 33]. As fog droplets impact this two-fibre-compound they quickly form liquid columns; further incoming fog water droplets intercepted by the wet co-fibres directly coalesce with the liquid column. As a result, no drop growth is observable (cf. figure 4 (d)). We perform experiments with both single fibres, of diameter d,

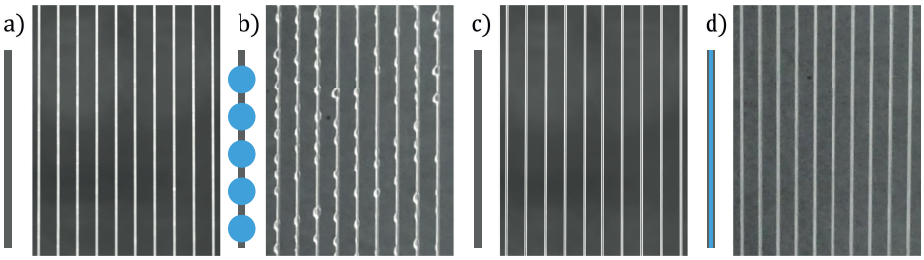

Figure 4: Photographs of the liquid collection on a net of 10 fibres with $d = 400\mu m$ (a) dry (b) wetted by the incoming fog, and of the liquid collection on a net of 10 co-fibres with $d' = 200\mu m$, and thus an equivalent pair diameter $d = 2d' = 400\mu m$ (c) dry and (d) wetted by the incoming fog . One can observe that in difference to b) there is no drop growth and that the separate fibres stick together to form a two-fibre-compound once they are wet, as sketched next to the photographs.

and pairs of fibres of equivalent diameter d, i.e. such that the sum of each diameter d' of the fibre in the pair is $2d' = d$. Although starting with small gaps between the fibres, when wetted, the fibres touch each other (4 (d)). We set the fibre spacing $e = 5$ mm to ensure $s < 0.08$, and measure the collected rate for various diameters d and varying velocities $0.6 < U < 2.5$ m/s. We plot the efficiency as a function of Stokes number (Fig. 5), and compare it to the inertial impaction model equations (6). Contrary to the case of a superhydrophilic fiber for which the collection efficiency follows equations (6) [30], the model significantly overestimates the efficiency for our experiments. This discrepancy can be rationalized by the fact that the drop distribution plays an important role on the capture mechanism [21]. Indeed, it affects both the collection surface, which is the liquid surface S_c (e.g. the projected surface of the drop) rather than the fibre surface, and the width of the obstacle around which the incoming droplets have to pass d_{obs}, (e.g. the drop diameter rather than the fibre diameter), which thus changes the Stokes number. We note that for a given fibre diameter and flow velocity, i.e. a given Stokes number, the collection is higher on liquid columns than on droplets. Following [21], we can build a model that takes into account the liquid distribution. We thus can define the efficiency as

$$\mathcal{E}' = \frac{Q_c}{qS_c} \tag{11}$$

and the Stokes number as

$$St' = \frac{\rho_d d_d^2 U}{9\mu d_{obs}}. \tag{12}$$

On single fibres, the liquid forms drops sitting on the fibres. Due to a growth and coalescence process of the drops on the fibres, as investigated in [21], for most of the collection process the drops are uniformly distributed along the fibre surface. The drops have an average size given by a balance between gravity and capillarity $d_D = \left(6\ell_c^2 \Delta\cos(\theta) d\right)^{1/3}$, where $\ell_c = \sqrt{\gamma/(\rho_d g)}$ is the capillary length and $\Delta\cos(\theta)$ is the contact angle hysteresis ($\Delta\cos(\theta) = 0.23$ for the nylon fibres

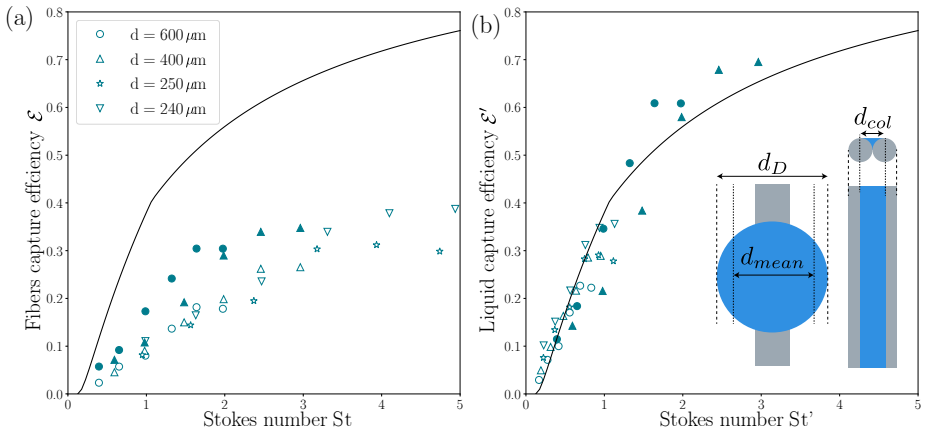

Figure 5: (a) Fibers efficiency $\mathcal{E}$ as a function of Stokes Number St. (b) Modified efficiency $\mathcal{E}'$ as a function of the modified Stokes Numbers St'. Experimental data for single fibres (drop growth, empty symbols) and co-fibres (columns, filled symbols) of equivalent diameter, for various diameters ($d = 240, 250, 400$ and 600 μm). Solid line: theoretical model equations (6).

used in our experiments), and are evenly spaced such that the number of drops present on the fibres is $N_d = L/(2\ell_c)$. We can thus define the collection surface as the surface of the drops

$$S_c = NN_d\pi(d_D/2)^2 = S_f d^{-1/3}\frac{9\pi L\ell_c^{1/3}\Delta\cos(\theta)}{16} \tag{13}$$

The average obstacle size is the drop mean diameter $d_{obs} = \pi d_D/4$ (cf. inset in figure 5). We note that the surface of the drops is always smaller than the surface of the fibres, i.e. the collection efficiency is lower, and the drop mean diameter is always larger than the fibre diameter, i.e. the Stokes number is smaller, which again decreases the collection efficiency. For co-fibres and liquid columns, the collection surface is given by the surface of the liquid column. The apparent column diameter is given by $d_{col} = \alpha d$, where α depends on the distance between the two co-fibres [32]; here, we assume the fibres are touching and $\alpha \simeq 0.5$ (cf. inset in figure 5). We have thus

$$S_c = NLd_{col} = \frac{S_f}{2} \tag{14}$$

and, as there are no drops exceeding the fibres, the obstacle diameter is $d_{obs} = d$ (cf. inset figure 5), and the Stokes number remains unchanged.

With these new definitions of the Stokes number and efficiency, our experimental data collapse onto a single line and are well described by the theoretical model (Fig. 5(b)). At equivalent fibre diameter, the collection efficiencies for the columns are always higher than the ones for drops, as it both increases the efficiency (through an increase of the collection surface) and maximizes the associated Stokes number (as the obstacle size remains restricted to the co-fibre diameter).

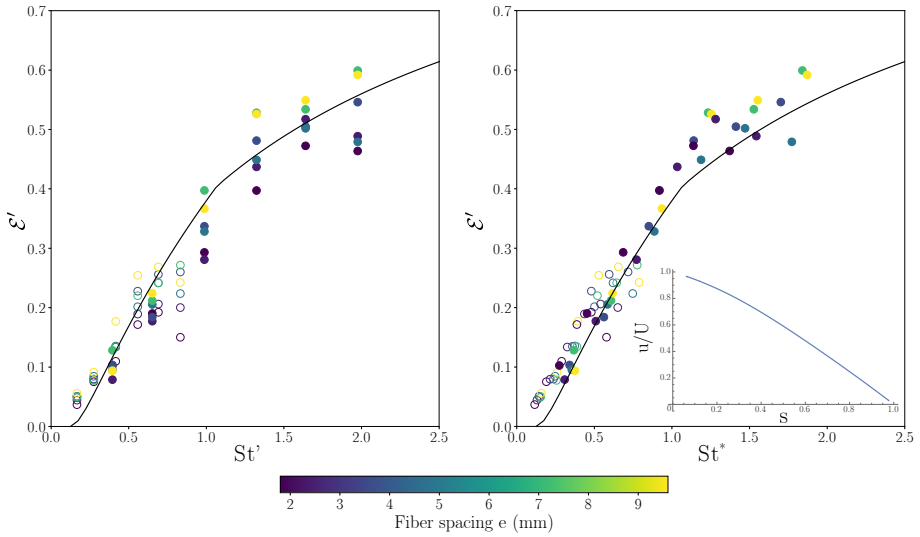

Figure 6: (a) Efficiency $\mathcal{E}'$ as a function of Stokes Number St' and (b) Efficiency $\mathcal{E}'$ as a function of the modified Stokes number St^*. Experimental data for the single fibres (drops, open symbols) and co-fibres (columns, filled symbols) of diameter $d = 600$ μm and different fibre spacings e (colorbar). Theoretical model equations (6) (solid line). Inset: Reduction of velocity due to flow deviations as a function of the solidity of the net s, line obtained from equations (15-16).

3.3. Aerodynamic effects

We now include aerodynamic effects by increasing the solidity of the net, i.e. decreasing the inter-fibre distance e. The measured efficiency is shown in figure 6. We observe that the efficiency decreases as the solidity increases, for both drops and columns, which indicates a significant blockage effect. In general, it is assumed that the main effect is the deviation of part of the fog around the obstacle [24, 25]. Here, we also consider the reduction of the normal velocity due to this blockage that will decrease the capture efficiency. The normal velocity in front of the net u, and thus the droplet incoming velocity, is not the infinite flow velocity ahead of the net U, but is reduced by a factor $u^* = u/U$ that depends on solidity. In order to determine this flow reduction, we use a recent analytical model of the flow through a porous plate [34] that extends previously described potential flow models [35, 36, 37]. The porous plate is modeled as a distribution of potential sources of uniform strength. The potential flow model is valid for high Reynolds numbers, as in our experiments where the Reynolds number is typically 10^6 - 10^7 (based on a characteristic length of the flow around the net, namely the net length). It is then possible to obtain the drag coefficient C_D which has two contributions, the total pressure drop due to the fluid circumventing the plate, and a further decrease of the total

pressure due to *base suction*, and may be expressed as

$$C_D = \frac{4}{3}\frac{(1-u^*)(2+u^*)}{(2-u^*)} \tag{15}$$

as a function of the reduced velocity. An additional equation is necessary to link u^* to the the drag coefficient and the solidity s. Calculating the total pressure loss on a streamline that passes through the plate as the sum of viscous losses due to the friction between the plate walls and the fluid particles, and dynamic losses due to separation of the flow at the end of the contraction gives [34]:

$$C_D = u^{*2}\left(\frac{1}{\phi^2}-1\right) - \frac{4}{3}\frac{(1-u^*)^3}{(2-u^*)^2}. \tag{16}$$

The drag coefficient increases with increasing solidity, and reaches a plateau for solid plates. Equating these two expressions for C_D (equations 15-16), we derive an expression for the dimensionless velocity reduction $u^*(s)$ (inset in Fig. 6(b)).

We can take into account this flow reduction in the Stokes number, i.e.

$$St^* = St' u^*(s) \tag{17}$$

Furthermore, we use the definition of $u^*(s)$ to determine the velocity reduction due to the pressure drop caused by the net in the wind tunnel as given by equation (7). For the highest solidity considered here, $u^*(s = 0.34) = 0.75$, this effect contributes to a reduction of velocity of 7.8%, while the total velocity reduction due to aerodynamics effects is 30.5%.

With this definition, all our data points fall onto a single line, which is well described by the theoretical model (cf. figure 6). The flow deviation due to blockage thus reduces the speed of incoming droplets and hence decreases the efficiency of the inertial capture mechanism, and this effect can simply be taken into account by modifying the Stokes number. The analytical model has been developed for two dimensional solid perforated plates, which differ from the actual configuration. We expect three-dimensional effects to affect the estimation of the velocity reduction, in particular the specific shape of the pores (i.e. parallel cylindrical fibers compared to a perforated plate) and the three-dimensional shape of the collector (in particular its aspect ratio). Furthermore, possible vibrations of the fibers could also lead to some errors. However, a detailed 3D model of the flow through and around a flexible net is beyond the scope of this paper, and the 2D model captures the main effects due to the net solidity as shown by the fair collapse of the data in Fig.6.

3.4. A universal model and an optimum for fog collection

We can now build a robust quantitative model for fog collection that takes into account the effect of the liquid distribution and of the net solidity through the collection surface S_c and the Stokes number St^*. Furthermore, flow deviations may occur around the net and some of the fluid does not reach the fibres (Fig. 1), which is generally the effect taken into account when considering an

aerodynamic efficiency [25]. In that case, the flux through the net is reduced to $q' = LWC \times U \times u^*(s)/\rho_d = qu^*(s)$ and thus depends on the solidity.

The collected flow rate is thus given by

$$Q_c = \mathcal{E}(St^*)q'S_c, \tag{18}$$

where $\mathcal{E} = \eta_c$ is the efficiency given by eqs. (6), the Stokes number St^* and the flux q' depend on the flow velocity and thus on the solidity through the velocity reduction u^*, and S_c depends on the liquid distribution, i.e. on the net geometry. The Stokes number can be written as

$$St^* = Hu^*(s)/d_{obs} \tag{19}$$

with a length

$$H = \frac{\rho_d d_d^2 U}{9\mu} \tag{20}$$

that is characteristic of the fog. In our laboratory experiments parameters are controlled making $H \sim 10^{-4}m$. In environmental fog, droplets sizes distribution is never unimodal and U and μ vary during an event (cf. next section). In Palaiseau, France or in Chile [20], H may vary from 10^{-4} to 10^{-2} m.

For a co-fibre collector, with fibre pairs of equivalent diameter d, the collection surface is $S_c = S_f/2 = sS_{net}/2$. Using (18),the net collection efficiency is thus

$$E = \frac{Q_c}{qS_{net}} = \frac{Q_c}{q'S_c}\frac{u^*(s)s}{2} = \mathcal{E}(St^*)\frac{u^*(s)s}{2} \tag{21}$$

i.e. we have

$$E = 0 \qquad \text{for } St^* < 0.125 \tag{22}$$

$$= 0.233su^* \left[\log_{10}\left(\frac{8Hu^*}{d}\right)\right]^2 \qquad \text{for } 0.125 < St^* < 1.1 \tag{23}$$

$$= \frac{Hsu^{*2}}{2d}\left(\frac{1}{Hu^*/d} + \pi/2\right) \qquad \text{for } St^* > 1.1 \tag{24}$$

The results obtained for a given fibre diameter, either as co-fibres or single fibres, and various incoming velocities (and thus fog characteristic H) is shown in Fig. 7. The model is in good agreement with the experimental data obtained on co-fibres, without any adjustable parameters. However, it tends to underestimate the values obtained in the wind tunnel at high velocities. This might come from an overestimation of the deviation effect, where we assumed that all the droplets carried by the deviated streamlines are lost; indeed, some of the droplets carried by the curved streamlines at the edges of the collector may still impact the wires and be collected.

As the solidity s increases, the collection surface S_c increases while the velocity u^* decreases, leading to an optimum for an intermediate solidity that depends on the fog characteristic H and the fibre equivalent diameter d. The shape of the curve, and thus the position of the optimum, depends on the Stokes

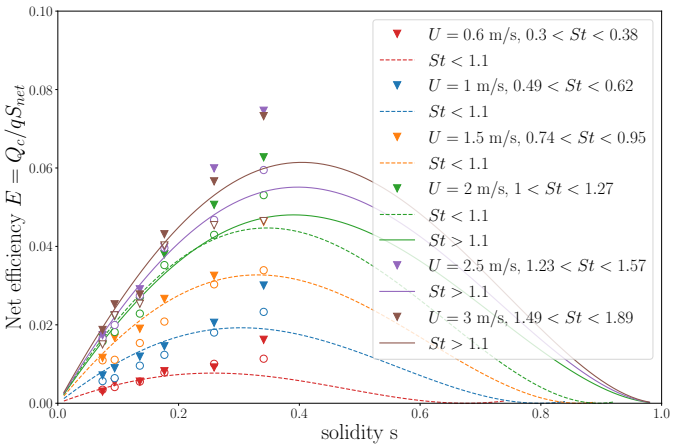

Figure 7: Efficiency of the net for liquid columns and drops as a function of the net solidity for single fibres (open circles) of diameter $d = 600\mu$m and co-fibres (filled triangles) of equivalent diameter $d = 600\mu$m (i.e. each fibre in the pair has a diameter $d' = 300\mu$m) and different flow velocities U, thus different values of H (colors). The Stokes number varies for a given U as the velocity decreases with increasing solidity, and the range of St is given in the caption. Dashed line: model equation (23), solid line: model equation (24).

number, and hence on the incoming velocity. As we increase the velocity, and thus the Stokes number, we change from equation (23) to equation (24). In addition, for a given incoming flow velocity U, the local Stokes number decreases with increasing solidity as the velocity in front of the net decreases, and we may switch from one expression to the other (see data for $U = 2$ m/s in Fig. 7). The collection rate presents an optimum between $0.3 < s < 0.5$ for the typical values used in our study. Close to the optimum (e.g. $s \gtrsim 0.5$), the inter-fibre distance is strongly reduced and liquid columns may start to form between each pair of fibres (so-called tangling in [38]), which changes both the collection surface and the obstacle width d_{obs}. We thus restrict our experiments to low solidities. In many systems, the nets or fog gauges have higher solidities. In particular, the Standard Fog Collector (SFC) consists in two layers of a woven mesh of solidity $s = 0.35$, giving an effective solidity of $0.5 < s < 0.75$ [39, 25]. At low wind speeds, the collection may actually be hindered at high solidities as the reduction of velocity leads to $St^* < 0.125$ for which no liquid is collected ($Q_c = 0$). There is thus a maximum solidity for collection, which is close to $s = 0.75$ for $U = 0.6$ m/s and increases with increasing velocity U to reach $s = 1$ for $U = 7.4$ m/s (Fig. 7). This may also explain some of the discrepancies in the events collected with different screens [15]. Furthermore, most fog gauges consist in two or three layers of wire arrays [12], leading to high apparent solidities for which we expect strong blockage and deviation effects, and thus a decrease in efficiency. In a recent study, measurements with multiple layers of low solidity

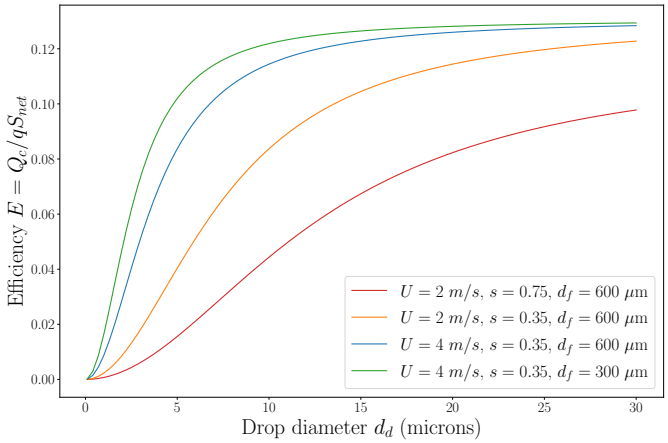

Figure 8: Efficiency of the net obtained theoretically (equation (24)) as a function of fog droplet diameters, for several wind speed, fiber diameter and solidities.

fibre arrays ($s = 0.17$) were performed [16]. In these experiments, first, an increase in collection rate for two to five layers was observed, followed by a slight decrease and saturation for a larger number of layers, i.e. larger apparent solidities, which is consistent with the model presented here. Finally, the effect of the fog characteristics and fiber diameter (i.e. changes in H) on the efficiency are shown in Fig. 8. The collection rate increases with decreasing fibre diameter (the finer the better). The efficiency is directly linked to the diameter of the fog droplets d_d, as the Stokes number is proportional to d_d^2; the higher the drop size, the higher the efficiency, as long as d_d remains small compared to the fiber size to remain in the inertial impact regime. These results could further help improve the design of active collectors that segregate drops by size by drawing fog at a given speed through several rows of wires [26].

4. In situ fog collector

We design a fog collector based on the results obtained in the laboratory, i.e. a low solidity array of co-fibres, in order to obtain an efficient collector whose collection rate may be compared to our model, and thus linked to the fog characteristics.

4.1. Design and study area

We build a large-scale rectangular fog collector net (width 2 m and height 1m), placed such that the surface center is 1m50 above the ground (Fig. 9). The net consists in one layer of parallel wires assembled by pairs to favor water column formation. Each wire is of 300 μm diameter, the co-fibre pairs are thus

Figure 9: Set-up for fog collection measurement, view from behind. An aluminum frame maintains 1380 pairs of parallel wires. A rain gauge is fixed below a tilted gutter. A cup anemometer is aligned with the center, 1m away from the installation. A wind vane is fixed on the top left corner of the supporting structure. Inset: zoom on the collector net charged with water, after a fog event. Primarily, water columns form on two pairs of wires, but a few drops are also observed.

$d = 600$ μm. The pairs are woven by hand along PVC plates drilled by laser cutting with a spacing of $e = 1.4$ mm between each pair (from center to center) (equivalent to $2.4d$) and thus a solidity $s = 0.41$, which is close to the optimal solidity defined previously. In total the rectangular frame maintains 2760 nylon fibres. We note that the tension in the wires is not homogeneous, but is sufficient for the pairs not to touch one another in dry condition without wind.

The set-up is in the SIRTA atmospheric research observatory in Palaiseau 25km southwest of Paris. Active and passive remote instruments and in situ sensors are operated here since 2002 [27]. The collector frame is aligned with the north as the main wind during fog season is a western wind. Moreover, the net faces a 1 km flat field in the East-West direction; a forest grows to the north; to the south there is a lake and high buildings (below 20m height). Higher wind speeds are therefore expected in the East-West direction as forest and buildings tend to obstruct and slow down the flow in contrast to the open field. We define the angle θ as the angle between the wind direction and the perpendicular to the net.

For near field measurements, we use four anemometers (two on each side of the collector) and a wind vane. Two anemometers are installed at 1.5 m above ground level (AGL), which is the same height as the collector center. The other two are installed at 2.3 m AGL. We assume that the wind speed is consistent

over the collector height. This assumption is acceptable for wind speeds above $1m/s$, as the collector is close to the ground and small compared to the boundary layer. To support this assumption we verify that upstream anemometers measure the same wind speed at 1.5 m and 2.3 m AGL. This assumption will not hold for larger or higher collectors. Wind speeds smaller than 1 m/s are not well measured with our instruments. In those cases we use high frequency measurements from a sonic anemometer. In addition, we use a rain gauge below the collector to collect intercepted water. Table 4.1 gives an overview of measured parameters, associated instruments, height position and sampling frequency. All the instruments are less than 500 m away from the collector. All the time indications are universal time (UT) and altitudes are above ground level (AGL).

Fog properties, formation and dissipation processes are an important part of the scientific research taking place within the site, and there is a large available literature (see for example [40, 41]). To track atmospheric conditions we rely on the SIRTA public data base using two instruments. First, fog induces a reduction of visibility, and a fog event is defined at a critical visibility $Vi_{max} = 1$ km. Above this value the event is not considered. Visibility is measured as a function of the line of sight of the visibility meter. Second, the fog monitor (DMT FM-120), installed at $4m$ AGL, measures the size distribution of droplets $n(d)$ between $d_{min} = 2\mu$m and $d_{max} = 50\mu$m. The Liquid Water Content (LWC) is obtained from this distribution as :

$$LWC = \int_{d_{min}}^{d_{max}} \frac{\pi \rho_d}{6} n(d) d^3 \mathrm{d}d. \tag{25}$$

There are two types of fog at SIRTA: radiation fog, that mostly occurs during the last five hours of the night, and stratus lowering fog that can happen after sunrise, typically in the afternoon [42, 43]. We only consider fog events that are not preceded or accompanied by rain, i.e. the rain gauge placed far from the collector does not collect any water a few hours before or during the event. Furthermore, we only consider the events for which all sensors are functioning in order to describe the fog microphysics. Out of 25 fog events recorded between December 2019 and early December 2021, we thus analyzed 12 events (no rain, all instruments on) that are reported in Table 2.

4.2. Fog collection

4.2.1. Typical fog events

A typical event is presented in Fig. 10. As the visibility decreases, the liquid water content increases, indicating the presence of fog (Fig. 10(a)). The collector indeed collects fog water, as seen by the increase in the collected volume V_c, while no rain is collected in the nearby rain gauge (Fig. 10(b)). The collection stops as the fog disappears. We note that throughout the fog event the wind velocity and direction varies (Fig. 10(c)). We obtain wind speed measurements with both upwind anemometers in the middle and on top of the net, as well

Instrument	Parameters	Frequency sampling	Height (m AGL)
Rain gauge - YOUNG 52202	Collected volume V_c	2ml tipping bucket	0
2 Cup anemometers PA2	Wind speed Ws	67 Hz at $30m/s$	1.5 2.5
Potentiometer PRV	Wind direction	0.2 Hz	2.30
Visibilimeter Degreane DF20+	Horizontal visibility V_i	0.02 Hz	4
FM120	Droplet size distribution Liquid Water Content Effectif diameter	1 Hz	2.5
Thermometer Guilcor PT100	Temperature	0.02 Hz	2
Rain gauge Precis Mecanique 3030	Rain quantity	5ml tipping bucket	0
Licor LI-7500, Sonic anemometer (METEK, CSAT3)	3 dimensional high frequency Ws	10 Hz	2

Instrument	Type	Range	Accuracy precision
Rain gauge - YOUNG 52202	tipping bucket		3% up to 1 L/hr
2 Cup anemometers PA2	Hall effect with magnets	0.5-60 m/s	0.5 m/s 1.5 2.5
Licor LI-7500, Sonic anemometer (METEK, CSAT3)	Sonic anemometer	4cm/s-60m/s	4cm/s

Table 1: Instrument and details resolution used in this study. All instruments are located at the SIRTA observatory main facility.

date and duration	$\langle LWC \rangle$ (g/m^3)	$\langle U \rangle$ (m/s)	$\langle \theta \rangle$ (°)	V_w (mL)	V_c (mL)	E	$\mathcal{E}'$	$\mathcal{E}^\dagger$	d_{eff} (μm)	St_{ed} range
07/01/20,7h35-9h35	0.0188	1.29	32	434.7	154.3	0.35	0.87	0.58	12.5 ± 5	0.54-14.1
07/01/20, 15h05 - 22h40	0.0212	1.48	60	1752	730	0.42	1.02	0.68	18 ± 2	0.45-31.1
26/01/20, 09h40-11h15	0.0290	1.1	49	518.8	105.7	0.2	0.495	0.33	15.2 ± 2.8	0.19-10
07/04/20, 3h10-6h10	**0.0006**	0.31	6.9	2.2	36.4	**16.5**			**3 ± 0.7**	0.04-0.2
11/11/20, 03h40 - 11h50	0.1106	1.11	**74**	7069	1828.6	0.26	0.63	0.42	14.9 ± 3	0.69-20.4
24/11/20, 2h30-9h30	0.0376	0.98	**76**	2698	1005.3	0.37	0.915	0.61	10 ± 4	0.26-20.4
26/11/20, 00h20-08h40	**0.0014**	0.41	19	55.6	444	**8**			**4 ± 0.7**	0.10-8.3
09/12/20, 15h20-18h15	0.0288	1.12	19	718	105.7	0.15	0.36	0.24	15.5 ± 2.5	0.42-11.6
11/12/20, 00h20-01h30	0.0163	1.28	**88**	220.2	51.4	0.23	0.57	0.38	16.8 ± 2.3	0.49-13.2
16/12/20, 00h30-11h30	0.0906	1.82	61	13258	3865.7	0.29	0.705	0.47	15 ± 3	0.84-23.3
27/01/21, 9h25-15h00	0.0361	1.68	19	2685	809.3	0.3	0.735	0.49	23 ± 2	0.4-23.7
19/02/21, 3h05-5h30	0.0406	1.7	60	1210.9	228.6	0.19	0.46	0.307	13.6 ± 2	0.2-4.61
07/12/21, 6h45-11h00	0.0342	2.5	60	2466.1	566.1	0.23	0.56	0.37	12.6 ± 2	1.6-4.8

Table 2: Fog events at SIRTA between 12/2019 and 12/2021.

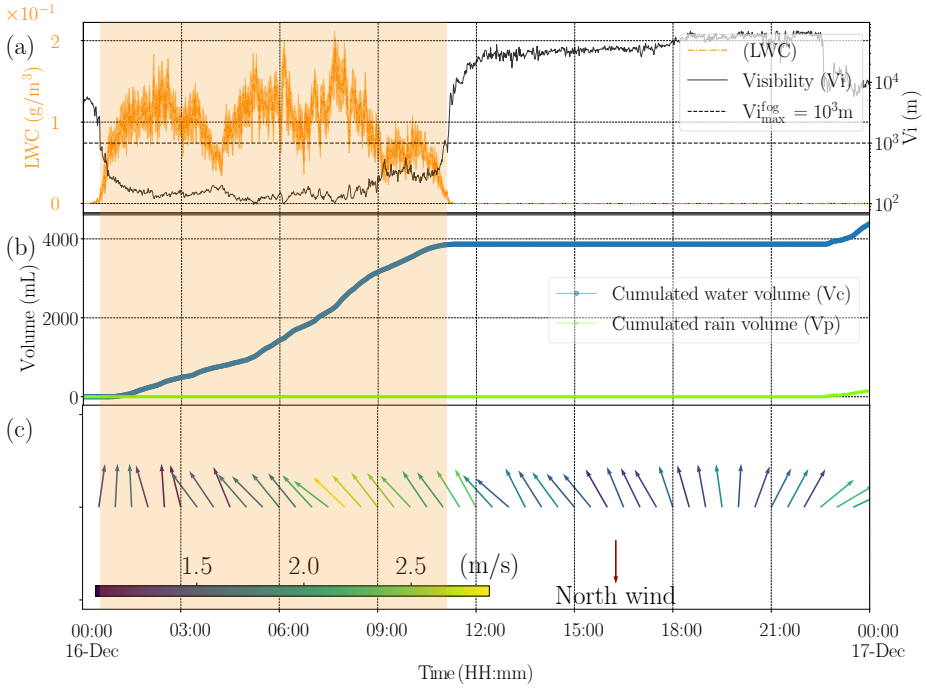

Figure 10: A typical fog event on 16/12/2020. (a) Evolution of the liquid water content (LWC, orange) and visibility (Vi, black). (b) Cumulated volume of collected water in the fog collector gauge (blue) and in the rain gauge (green). (c) Wind speed and direction.

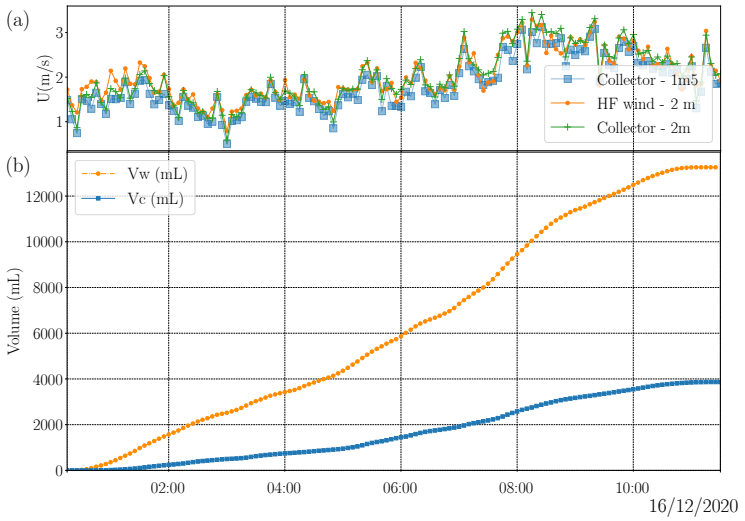

Figure 11: A typical fog event on 16/12/2020. (a) Evolution of the wind speed for three different anemometers. (b) Evolution of the collected volume V_c and of the estimated volume of water crossing the net V_w.

as with the high frequency anemometer attached on a mast located about 30 m from the net (Fig. 11 (a)). These results indicate that the wind is almost uniform along the net height, and that it is homogeneous across the field of the SIRTA. The liquid water content is measured about 60 meters behind the net at an altitude of 2.5 m. We assume that the fog is homogeneous in the entire field, and we average the measurements over a period of 5min (5 min being the time a droplet would need to be transported across 300 m by a wind speed of 1 m/s). We will then consider that the LWC measured with the FM120 is the LWC in front of the collector. The volume of water flowing through the collector from the beginning of the event t_0 to the end t_f is thus calculated as:

$$V_w = \int_{t_0}^{t_f} LWC \times U \times S_{net} \, \mathrm{d}t, \tag{26}$$

and the volume that may be collected, i.e. that will encounter the fibres, is defined as $V_{wf} = V_w s$, with a constant solidity $s = 0.41$. The cumulated water volume increases during one fog event, as shown in Fig. 11 (b). We see that, after a short delay, the collection of water by the net follows a similar trend as the volume of water that passes through the net. The delay between the beginning of the fog and the water collection depends on the event, and corresponds to the time needed for the wires to be wetted and the drainage to start. The rapid response of the net is well observed during a non uniform fog event as the one presented in Fig. 12. Here, three events follow one another; the different events can be clearly distinguished in the evolution of the volume of collected water (Fig. 12(a-b)). A first slope corresponds to the first event at

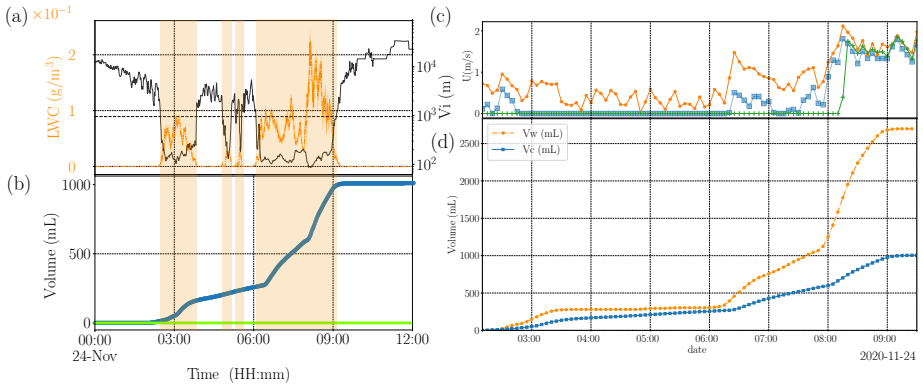

Figure 12: A non-uniform fog event on 24/11/2020: (a) LWC and visibility indicate several passages of fog, which are clearly observed in (b) the evolution of the volume of collected water. (c) Evolution of the wind speed and (d) V_c and V_w.

2h50; water then keeps on flowing, corresponding to the drainage of the water collected on the wires, as well as the brief passages of fog between 5h00 and 6h00. The slope then increases with a second fog event at 6h00, and increases further with a denser fog event at 8h00. During these different events, the wind velocity also varies (Fig. 12(c)). Indeed, the flow velocity is very low for the first events, and strongly increases for the last event. We note that the anemometers situated close to the net can not measure wind with a velocity < 0.5 m/s, and are thus not able to capture the low wind velocities of the first events. In these situations, we use the data obtained with the High Frequency Anemometer. As soon as the wind rises, all three anemometers give similar values (Fig. 12 (c)). From these measurements, we estimate the volume of fog water using eq. (26) as shown in Fig. 12(d). V_w indeed exhibits three phases, which are closely followed by the cumulated fog water collection volume V_c, with a short delay. This reflects the high sensitivity of our fog net. Furthermore, we see that the ratio of collected water to incoming water depends on the flow velocity, as in our laboratory experiments and as expected from the collection mechanisms.

4.2.2. Fog characteristics: Stokes number

We can further characterize the microphysics of the fog using the drop size distributions obtained with the FM120. The size distribution $n(d)$ obtained for the fog event presented in Figures 10 and 11 is presented in Fig. 13 (a); in addition, we can show the distribution in volume (Fig. 13 (b)). This distribution is typical of the distribution we measured for all considered fog events. There are two populations of drops: small droplets, of typical diameter around $d = 5 - 10$ μm, that are the most present in the fog, and larger droplets of diameter around $d = 20 - 30$ μm that represent the largest part of the fog. We can define the most frequent size $d_{max,N}$ as well as the dominant drop size $d_{max,vol}$ (Fig. 13). We can further define the median drop size, d_{mvd}, as well as the effective

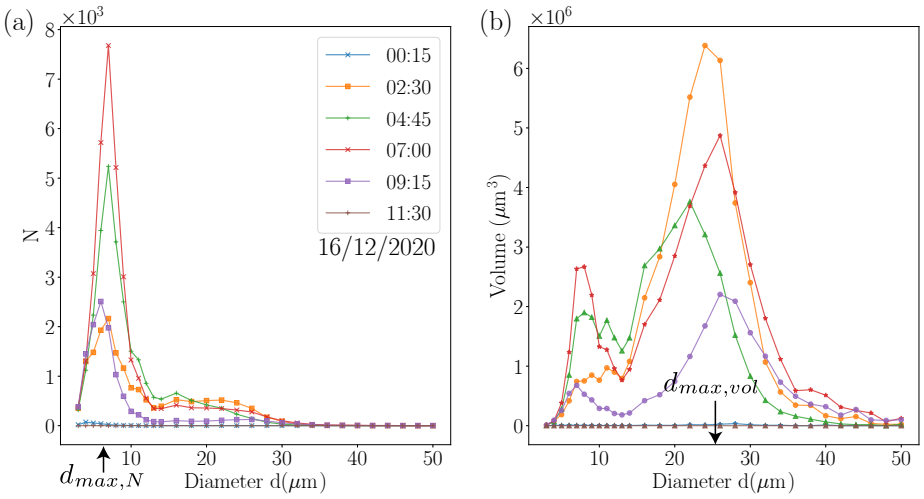

Figure 13: Drop size distribution in number (a) and in volume (b) at different times during the fog event on December 16th, 2020.

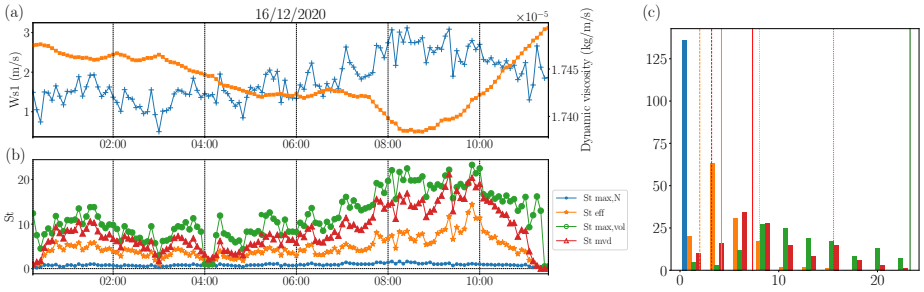

Figure 14: Fog event on December 16th, 2020: (a) Evolution of wind speed, dynamic viscosity and (b) Stokes numbers (c) Distribution of values for the Stokes numbers during the event.

diameter d_{eff} using the size distribution function such that

$$d_{eff} = \frac{\int_{d_{min}}^{d_{max}} n(d) d^3 \mathrm{d}d}{\int_{d_{min}}^{d_{max}} n(d) d^2 \mathrm{d}d}. \tag{27}$$

The drop distribution slightly evolves as the fog develops. In most fog events, the two droplet sizes are present and the effective diameter remains close to $d_{eff} = 15$ μm (Table 2). We can thus define four Stokes numbers based on these various typical drop sizes: $d_{max,N}$, $d_{max,vol}$, d_{mvd}, and d_{eff}. Furthermore, the wind velocity and the fog temperature, and thus the fluid viscosity, evolve with time during one event (Fig. 14 (a)); we can thus define the four Stokes numbers at each time (Fig. 14 (b)). For each event, we plot the distribution of Stokes numbers (Fig. 14 (c)). The Stokes number associated with $d_{max,N} \simeq 5$ μm is typically small, and in general $\lesssim 0.5$. As $d_{max,vol} \simeq 25$ μm, the associated Stokes

number is larger and varies with the wind velocity, with a typical amplitude $0.5 < St_{max,vol} < 25$. The distribution is broad with a peak that is not well defined. The median Stokes number has the same range, with a slightly more pronounced peak at smaller values (as it includes the small droplets). Finally, the Stokes number based on the effective diameter has a narrower distribution, with a better defined peak at a value closer to unity $1 \lesssim St_{eff} \lesssim 4$. For the mean and effective Stokes we also report the 10th and 90th percentile values.

4.2.3. Low density events

We also record very low LWC fog events (see bold values in Table 2). One of these events is described in Fig. 15. For most of the event, the LWC remains below 10^{-2}g/m^3, and the wind velocity is less than 1 m/s. The cumulative estimated volume of water in the fog is low (a few mL). These events are well captured by the collector, which actually collects important volumes of water. The cumulative volume of collected water largely exceeds the estimated V_w, which will lead to absurd values for the efficiency. These events are characterized by a droplet size distribution that only exhibits small droplets, which explains the low values of the LWC. One hypothesis would be that the Fog Monitor does not reflect the actual size of droplets present in the fog; drops larger than the FM120 range (i.e. larger than 50 μm) may be present in the fog. Another hypothesis would be that the fog is denser at the height of the collector ($2m$ AGL) and quickly dissipates at $4m$, where the FM120 measurements are performed. These results also indicate that our passive fog collector is a robust measurement method for fog content close to the ground, even for short, low-speed, and low-LWC events.

4.2.4. Collection efficiency

As we have seen, the fog collection is not constant over the duration of a single fog event, due to variations in LWC and wind speed U. However, as a first step, we can define an efficiency for a given fog event based on the cumulated collected volume as

$$E = \frac{V_c}{V_w} \tag{28}$$

We may also define the efficiency with the average flow rates. The collected flow rate is computed as the integration of the collected volume from the beginning of the collection process to the last bucket tipping, while the fog flow rate is computed as the integration of V_w from the beginning of the fog event to the end. Both methods give similar results. We compute the efficiency using the first method for all events recorded at SIRTA (excluding events with rain or where instruments such as FM120 were failing), as the second one is heavier to compute. The computed values for the efficiency E is in the range $0.15 < E < 0.37$ (Table 2). However, in order to compare with the theoretical model and the laboratory experiments we need to consider the fibers capture efficiency, i.e. compare the collected volume to the amount that reaches the fibres $V_{wf} = V_w s$, or the efficiency $\mathcal{E} = E/s$. We compute very high efficiencies that can be larger than one, which indicates an overestimation of the collection surface (Table 2).

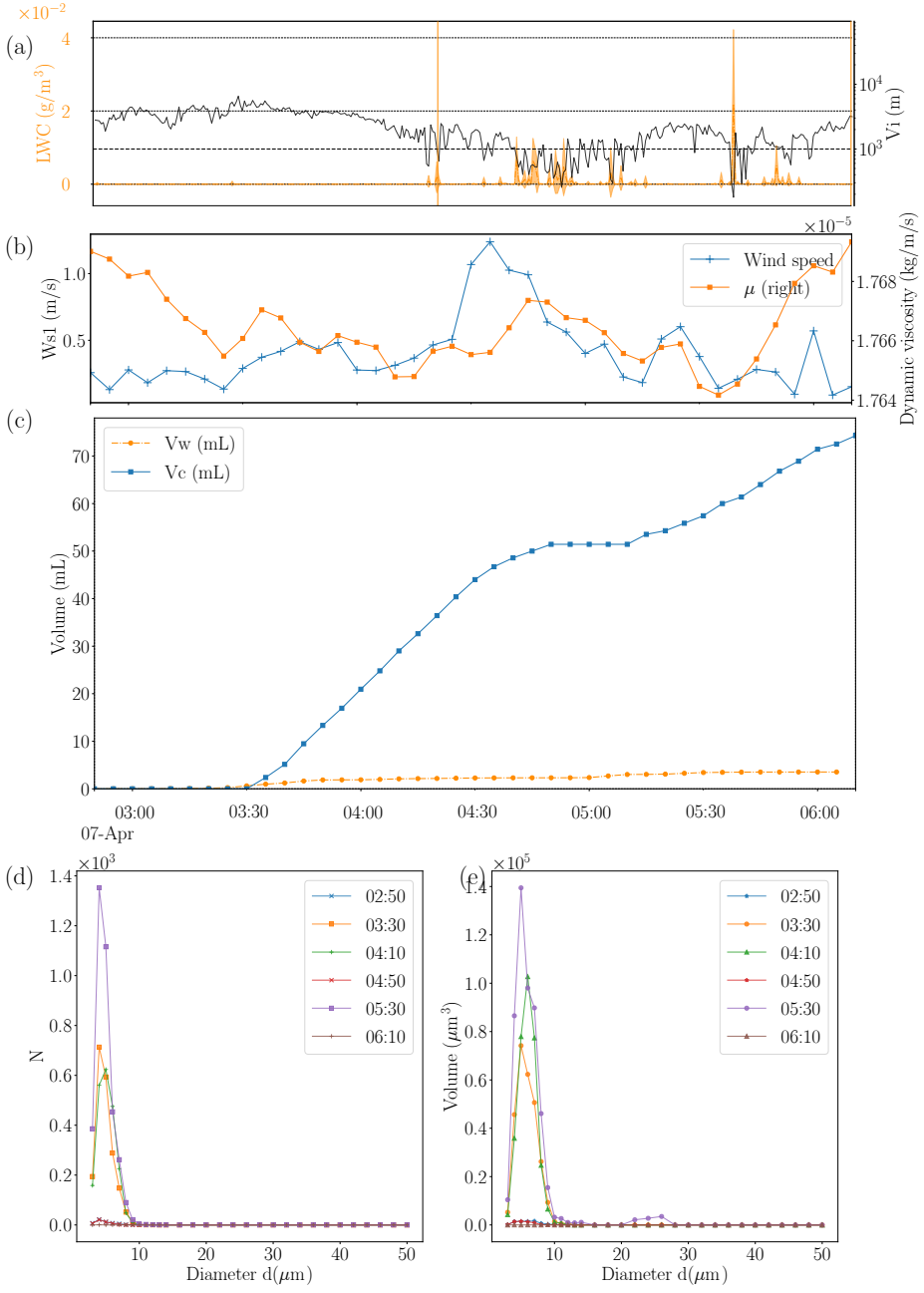

Figure 15: A low density fog event: (a) Visibility and LWC, (b) Wind velocity and viscosity, (c) Collected volume V_c and estimated fog water volume V_w, (d-e) Droplet size distributions in number and volume.

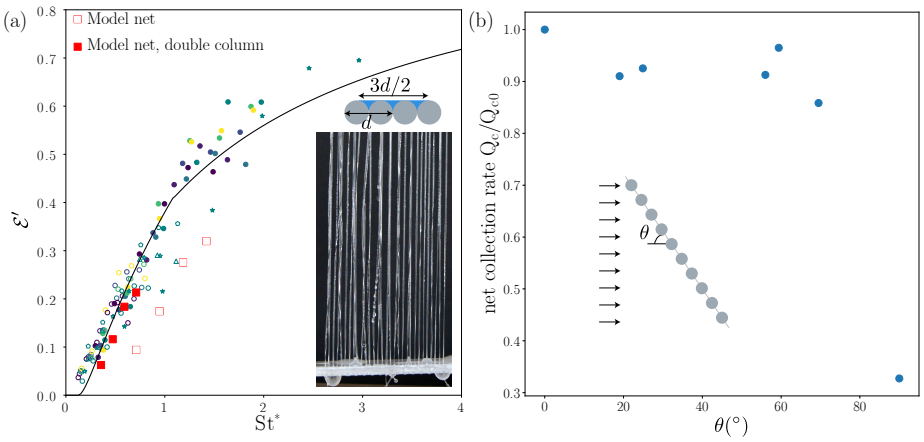

Figure 16: (a) Efficiency as a function of Stokes number for a sample of the net (red squares): empty symbols with the definitions of $\mathcal{E}'$ and $St*$, filled symbols with the definition with double-columns $\mathcal{E}^\dagger$ and $St^\dagger$. Inset: Picture of the sample net in the fog wind tunnel showing double columns. Experiments on single and co-fibres (colored symbols) corresponding to the ones shown in Fig. 6, Model eqs(6) (plain line). (b) Evolution of collection rate as a function of the net angle θ, normalized by the collection rate at $\theta = 0$. Experiments performed with co-fibres of equivalent diameter $d = 600\mu$m, for a net of solidity $s = 0.34$ and at a velocity $U = 3$ m/s.

Indeed, when observing the net, we see that columns mostly form between co-fibre pairs, i.e. assembling four fibres instead of two (Fig. 9). This is due to the inter-fibre distance being close to the capillary length for our net solidity ($s = 0.41$). At this distance, drops may bridge adjacent fibre pairs, especially thanks to the motion of fibres with the wind. Furthermore, as the fibres are flexible and not kept under high tension, they may form bundles with adjacent fibres due to the capillary forces exerted by the drops bridging the fibres [44, 45, 38]. We perform experiments on a smaller net with the same characteristic as the in situ net in our wind tunnel, with loose fibres separated by the same distance (using the same drilled PVC plates). In the lab, the columns also form between two pairs of co-fibres (inset in Fig. 16). We record the collection efficiency as a function of the Stokes number as defined in our laboratory experiments (Fig. 16 (a)).The data points (open red squares) actually lie below the curve. The collection surface is the one on 2 co-fibres (inset in Fig. 16 (a)), which we can estimate as $S_{c,c} = NL(3/2)d$, and the size of the obstacle is now $d_{obs} = 2d$. This effectively reduces the efficiency by a factor 2/3 and decreases the Stokes number by a factor 2; the data points with this new calculated values $\mathcal{E}^\dagger = (2/3)\mathcal{E}'$ and $St^\dagger = St^*/2$ (filled red squares) lie on the line obtained with the previous controlled experiments as well as the theoretical prediction, with an excellent agreement. This again indicates that taking into account the liquid distribution on the fibre is paramount to quantify the efficiency of the collecting net.

While the orientation of the wind evolves throughout an event, we may define an average orientation θ with respect to the perpendicular to the net.

For most events, this angle varies between 6 and 60°, while some events present average directions closer to 90° (see bold values in Table 2). Previous studies with mesh-like collectors have considered the effect of the wind angle in the projected surface of the net, thus defining the volume of water flowing through the mesh $V_w = LWC\ U\ S_{net}\ \cos\theta$ [20], and therefore considering an effect of the orientation angle on the efficiency. However, for a collection of cylindrical fibers, the apparent surface of the fibers $S_f = NLd$ does not depend on the orientation angle θ. The decrease of the total projected area of the net nevertheless leads to an increase of the apparent solidity, thus increasing deviations of the fog around the net and decreasing the collection rate. We perform laboratory-scale experiments on a co-fibre net of solidity $s = 0.34$ (Fig. 16)(b)). The collection rate is only slightly affected by the angle, except close to 90°. There is a slight decrease in collection rate, consistent with the increase of apparent solidity, but for angles lower than 75°, the collection rate is still 85% of the nominal value at 0°. We thus consider that the angle does not play a role in the capture efficiency $\mathcal{E}$ for our nets. Indeed, the collection efficiency of high angle events is not significantly lower than the other efficiencies with similar wind speeds and LWC (Table 2). The increase in apparent solidity, and thus the effect of the orientation angle, may however be important at higher net solidities.

In order to compare these results to our laboratory experiments and model, we plot the efficiency as a function of Stokes number for the in situ collector (Fig. 17). Each event is characterized by a single efficiency; we thus neglect transient effects that may be important, in particular here as fog events in Palaiseau are generally short, with varying densities and wind speed. These variations in wind speed during a single event may lead to high variations of the instantaneous efficiency. Furthermore, for a given event the Stokes number can be estimated with several definitions based on the capture of different drop sizes, and therefore varies within a wide range. The situation may be different in regions where fogs are more homogeneous and long lasting, e.g. in Chile or Morocco, and as experimented in our wind tunnel. Nevertheless, these results may help inform on the droplet sizes involved in the collection.

The values for the efficiencies all lie within the range expected for Stokes number between 0.5 and 4 (Fig. 17). However, the data does not show a clear trend with the Stokes number. Small droplets, albeit being dominant in the drop distribution, are characterized by a small Stokes number and mainly do not seem to contribute to the collection. The evolution of efficiency with the Stokes number based on the size of the large droplets gives a clearer trend. In addition, the Stokes value based on average drop size is closer to the value obtained in our model laboratory experiments and theoretical model, indicating that all drop sizes may be captured and contribute to the final efficiency. These results are consistent with the evolution of the efficiency with droplet size presented in Fig. 8: small drops (5 μm) lead to small efficiencies, in particular in our wind speed range, while drops between 15 and 30 μm are collected with similar efficiencies. Finally, the Stokes number based on the effective drop size, while being in the correct range, does not provide a discriminating value that could help organize the efficiencies of the different events.

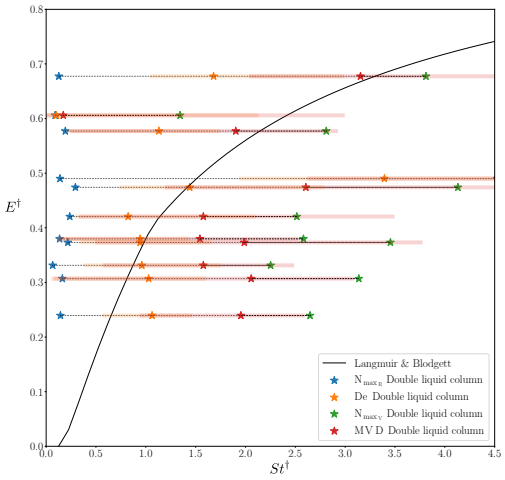

Figure 17: Efficiency of the in situ net as a function of Stokes number: $St_{max,n}$ which represents the most numerous drop size in the fog (small droplets), $St_{max,vol}$ which represent the most important drop size (large drops), St_{mvd} which represents the mean drop size, and St_{ed} based on the effective drop size. The points represent the peak of the Stokes histogram, while the shaded area represents the width of the distribution (between 10% and 90%).

To summarize, our fog collector indeed collects all fog events, even the events associated with low wind speed and low LWC; in fact, our results are reliable even when the fog monitor (FM120) does not detect large quantities of fog. The efficiency of collection varies between 20% and 70%, in agreement with the expected values associated with fog characteristics in Palaiseau. However, linking the efficiency to the fog microphysics remains challenging, in particular due to the high variability of the wind velocity (thus Stokes number), drop size and LWC during a single event. While our collector reacts quickly to changes in fog characteristics, as highlighted by the mirrored evolution of collected water and incoming water flux, one needs to better characterize the drainage dynamics, and the offset observed between fog passage and collection in the gutter/rain gauge, in order to compare the instantaneous collection to the local fog characteristics. The evolution of the average efficiency as a function of Stokes number indicates that all droplet sizes are captured by the collector, although small droplets do not contribute significantly to the collection. In particular, using an effective drop radius to estimate the Stokes number gives the correct range of values but does not explain the variations in efficiencies between different events.

5. Conclusion

Using controlled laboratory experiments, we quantitatively characterize the fog collection on assemblies of parallel wires. A small change of structure, using

co-fibres pairs rather than single fibres, improves the collection efficiency of the collector. We build a predictive model, without adjustable parameters, that quantitatively describes our experimental data. Based on these results, we design and build a large scale fog collector that collects environmental fog in Palaiseau, France. We propose a method to accurately evaluate the efficiency of our collector, with simultaneous measurements of collected water volume and fog characteristics. Our passive net collects all events, with efficiencies ranging from 20 to 70% depending on the fog characteristics. The link between meteorological data and collection efficiency may be improved by considering shorter fibres with a faster response time allowing for a more precise description of transient collection dynamics, to better describe the variability of fog events. While our model suggests an optimum for fog collection around a solidity of $s = 0.4$, our experimental results show that nets may experience bundling of the fibres for such solidities, leading to a reduced efficiency. The fog gauges and nets typically used nowadays present even higher solidities, at which both clogging and important aerodynamic deviations may occur. Lower solidity nets may in fact present better efficiencies. Indeed, with relatively low density fogs $LWC \sim 0.02$ g/m^3, and low wind speeds $U < 2$ m/s, our simple low solidity net consisting in a single layer of spaced co-fibres collects on average 50% of the incoming fog. In a region of high density fogs, such as in Morocco and Chile, with $LWC \sim 0.5$ g/m^3 and high wind speeds $U > 5$ m/s, this simple net could provide large values of collected water. Note that the efficiency depicted here is the fibers collection efficiency $\mathcal{E}$, i.e. based on the surface of the fibers, and not the overall net efficiency E based on the surface of the entire net with is 30% lower for the solidity considered here. However, for our array of parallel fibers, the relevant value is not necessarily the yield per square meter but the yield per number of fibers, as the cost of the collector may be linked to the amount of used wires rather than the surface of the net. Furthermore, the low solidity arrays of fibers exhibit a smaller drag coefficient that high solidity meshes, and thus may be larger without structural issues nor tearing (as no tension is transmitted between the wires contrary to a knitted mesh). Overall, our system of co-fibers present several advantages. In particular, it allows to optimize yield by creating super-hydrophilic fibers with a purely geometric solution, independently of the materials of the fibers, i.e. without any treatment (which might be costly and non durable) or specific material. Furthermore, this design could help improve the reliability of fog gauges; all the detected fog events led to water collection, even short, low-speed, and low-LWC events. Changes in the characteristics of the fog (increase in wind speed, variation of LWC) led to distinct variations in the collected water flow rate. In addition, the efficiency of the parallel fibers net is independent on the incoming angle of the wind. Our passive low solidity co-fibre collector thus gives an accurate and robust description of all fog events, and provides a cost-effective optimal solution for fog harvesting nets.

Acknowledgements

We thank Romain Labbe and Xavier Amandolese for their help designing and building the fog collector, as well as Jean-Charles Dupont and Johan Parra for help with the intrumentation of the collector and installation at the SIRTA site.

References

[1] V. A. Mohnen, J. A. Kadlecek, Cloud chemistry research at Whiteface Mountain, Tellus B 41B (1) (1989) 79–91. doi:10.1111/j.1600-0889.1989.tb00127.x.
URL http://www.tellusb.net/index.php/tellusb/article/view/15052

[2] R. S. Schemenauer, P. I. Joe, The collection efficiency of a massive fog collector, Atmospheric Research 24 (1-4) (1989) 53–69. doi:10.1016/0169-8095(89)90036-7.
URL https://linkinghub.elsevier.com/retrieve/pii/0169809589900367

[3] O. Klemm, R. S. Schemenauer, A. Lummerich, P. Cereceda, V. Marzol, D. Corell, J. van Heerden, D. Reinhard, T. Gherezghiher, J. Olivier, P. Osses, J. Sarsour, E. Frost, M. J. Estrela, J. A. Valiente, G. M. Fessehaye, Fog as a Fresh-Water Resource: Overview and Perspectives, AMBIO 41 (3) (2012) 221–234. doi:10.1007/s13280-012-0247-8.
URL http://link.springer.com/10.1007/s13280-012-0247-8

[4] R. Ghosh, R. Ganguly, Fog harvesting from cooling towers using metal mesh: Effects of aerodynamic, deposition, and drainage efficiencies, Proceedings of the Institution of Mechanical Engineers, Part A: Journal of Power and Energy 234 (7) (2020) 994–1014. doi:10.1177/0957650919890711.
URL http://journals.sagepub.com/doi/10.1177/0957650919890711

[5] J. Joslin, S. Mueller, M. Wolfe, Tests of models of cloudwater deposition to forest canopies using artificial and living collectors, Atmospheric Environment. Part A. General Topics 24 (12) (1990) 3007–3019.

[6] P. Herckes, P. Mirabel, H. Wortham, Cloud water deposition at a high-elevation site in the Vosges Mountains (France), Science of The Total Environment 296 (1-3) (2002) 59–75. doi:10.1016/S0048-9697(02)00037-2.
URL https://linkinghub.elsevier.com/retrieve/pii/S0048969702000372

[7] A. Ritter, C. M. Regalado, G. Aschan, Fog Water Collection in a Subtropical Elfin Laurel Forest of the Garajonay National Park (Canary Islands): A Combined Approach Using Artificial Fog Catchers and a Physically Based Impaction Model, Journal of Hydrometeorology 9 (5) (2008)

920–935. doi:10.1175/2008JHM992.1.
URL http://journals.ametsoc.org/doi/10.1175/2008JHM992.1

[8] R. E. Falconer, P. D. Falconer, Determination of cloud water acidity at a mountain observatory in the Adirondack Mountains of New York State, Journal of Geophysical Research: Oceans 85 (C12) (1980) 7465–7470. doi:10.1029/JC085iC12p07465.
URL http://doi.wiley.com/10.1029/JC085iC12p07465

[9] R. S. Schemenauer, Acidic deposition to forests: The 1985 chemistry of high elevation fog (CHEF) project, Atmosphere-Ocean 24 (4) (1986) 303–328. doi:10.1080/07055900.1986.9649254.
URL http://www.tandfonline.com/doi/abs/10.1080/07055900.1986.9649254

[10] J. O. Juvik, P. C. Ekern, WRRCTR No. 118 A Climatology of Mountain Fog on Mauna Loa, Hawai'i Island, Tech. Rep. WRRCTR No. 118, Water Resources Research Center, University of Hawaii at Manoa (1978).

[11] C. M. Regalado, A. Ritter, The performance of three fog gauges under field conditions and its relationship with meteorological variables in an exposed site in Tenerife (Canary Islands), Agricultural and Forest Meteorology 233 (2017) 80–91. doi:10.1016/j.agrformet.2016.11.009.
URL https://linkinghub.elsevier.com/retrieve/pii/S016819231630435X

[12] C. M. Regalado, A. Ritter, On the estimation of potential fog water collection from meteorological variables, Agricultural and Forest Meteorology 276-277 (2019) 107645. doi:10.1016/j.agrformet.2019.107645.
URL https://linkinghub.elsevier.com/retrieve/pii/S0168192319302539

[13] C. Schunk, P. Trautwein, H. Hruschka, E. Frost, L. Dodson, A. Derhem, J. Bargach, A. Menzel, Testing Water Yield, Efficiency of Different Meshes and Water Quality with a Novel Fog Collector for High Wind Speeds, Aerosol and Air Quality Research 18 (1) (2018) 240–253. doi:10.4209/aaqr.2016.12.0528.
URL https://aaqr.org/articles/aaqr-16-12-fog-0528

[14] C. M. Regalado, A. Ritter, The design of an optimal fog water collector: A theoretical analysis, Atmospheric Research 178-179 (2016) 45–54. doi:10.1016/j.atmosres.2016.03.006.
URL https://linkinghub.elsevier.com/retrieve/pii/S0169809516300564

[15] D. M. Fernandez, J. Kleingartner, A. Oliphant, M. Bowman, A. Torregrosa, P. S. Weiss-Penzias, B. J. Zhang, D. Sorensen, R. E. Cohen, G. H. McKinley, Fog Water Collection Effectiveness: Mesh Intercomparisons, Aerosol and Air Quality Research 18 (1) (2018) 270–283. doi:

10.4209/aaqr.2017.01.0040.
URL https://aaqr.org/articles/aaqr-17-01-fog-0040

[16] M. Azeem, A. Guérin, T. Dumais, L. Caminos, R. E. Goldstein, A. I. Pesci, J. de Dios Rivera, M. J. Torres, J. Wiener, J. L. Campos, J. Dumais, Optimal Design of Multilayer Fog Collectors, ACS Applied Materials & Interfaces 12 (6) (2020) 7736–7743. doi:10.1021/acsami.9b19727.
URL https://pubs.acs.org/doi/10.1021/acsami.9b19727

[17] J. Knapczyk-Korczak, P. K. Szewczyk, D. P. Ura, K. Berent, U. Stachewicz, Hydrophilic nanofibers in fog collectors for increased water harvesting efficiency, RSC Advances 10 (38) (2020) 22335–22342. doi:10.1039/D0RA03939J.
URL http://xlink.rsc.org/?DOI=D0RA03939J

[18] J. Li, R. Ran, H. Wang, Y. Wang, Y. Chen, S. Niu, P. E. Arratia, S. Yang, Aerodynamics-assisted, efficient and scalable kirigami fog collectors, Nature Communications 12 (1) (2021) 5484. doi:10.1038/s41467-021-25764-4.
URL https://www.nature.com/articles/s41467-021-25764-4

[19] J. Park, C. Lee, S. Lee, H. Cho, M.-W. Moon, S. J. Kim, Clogged water bridges for fog harvesting, Soft Matter 17 (1) (2021) 136–144. doi:10.1039/D0SM01133A.
URL http://xlink.rsc.org/?DOI=D0SM01133A

[20] S. Montecinos, D. Carvajal, P. Cereceda, M. Concha, Collection efficiency of fog events, Atmospheric Research 209 (2018) 163–169. doi:10.1016/j.atmosres.2018.04.004.
URL https://linkinghub.elsevier.com/retrieve/pii/S0169809517310219

[21] R. Labbé, C. Duprat, Capturing aerosol droplets with fibers, Soft Matter 15 (35) (2019) 6946–6951. doi:10.1039/C9SM01205B.
URL http://xlink.rsc.org/?DOI=C9SM01205B

[22] K.-C. Park, S. S. Chhatre, S. Srinivasan, R. E. Cohen, G. H. McKinley, Optimal Design of Permeable Fiber Network Structures for Fog Harvesting, Langmuir 29 (43) (2013) 13269–13277. doi:10.1021/la402409f.
URL https://pubs.acs.org/doi/10.1021/la402409f

[23] E. Bresci, Wake characterization downstream of a fog collector, Atmospheric Research 64 (1-4) (2002) 217–225. doi:10.1016/S0169-8095(02)00093-5.
URL https://linkinghub.elsevier.com/retrieve/pii/S0169809502000935

[24] J. d. D. Rivera, Aerodynamic collection efficiency of fog water collectors, Atmospheric Research 102 (3) (2011) 335–342. doi:10.1016/j.atmosres.2011.08.005.

URL https://linkinghub.elsevier.com/retrieve/pii/S0169809511002559

[25] D. Carvajal, L. Silva-Llanca, D. Larraguibel, B. González, On the aerodynamic fog collection efficiency of fog water collectors via three-dimensional numerical simulations, Atmospheric Research 245 (2020) 105123. doi:10.1016/j.atmosres.2020.105123.
URL https://linkinghub.elsevier.com/retrieve/pii/S0169809520310590

[26] B. Demoz, J. Collett Jr, B. Daube Jr, On the caltech active strand cloud-water collectors, Atmospheric research 41 (1) (1996) 47–62.

[27] M. Haeffelin, L. Barthès, O. Bock, C. Boitel, S. Bony, D. Bouniol, H. Chepfer, M. Chiriaco, J. Cuesta, J. Delanoë, P. Drobinski, J.-L. Dufresne, C. Flamant, M. Grall, A. Hodzic, F. Hourdin, F. Lapouge, Y. Lemaître, A. Mathieu, Y. Morille, C. Naud, V. Noël, W. O'Hirok, J. Pelon, C. Pietras, A. Protat, B. Romand, G. Scialom, R. Vautard, SIRTA, a ground-based atmospheric observatory for cloud and aerosol research, Annales Geophysicae 23 (2) (2005) 253–275. doi:10.5194/angeo-23-253-2005.
URL https://angeo.copernicus.org/articles/23/253/2005/

[28] R. Mead-Hunter, A. J. King, B. J. Mullins, Aerosol-mist coalescing filters – A review, Separation and Purification Technology 133 (2014) 484–506. doi:10.1016/j.seppur.2014.06.057.
URL https://linkinghub.elsevier.com/retrieve/pii/S1383586614004092

[29] I. Langmuir, K. Blodgett, A mathematical investigation of water droplet trajectories, Vol. 5418, Army Air Forces Headquarters, Air Technical Service Command, 1946.

[30] Y. Jiang, S. Savarirayan, Y. Yao, K.-C. Park, Fog collection on a superhydrophilic wire, Applied Physics Letters 114 (8) (2019) 083701.

[31] W. Shi, M. J. Anderson, J. B. Tulkoff, B. S. Kennedy, J. B. Boreyko, Fog Harvesting with Harps, ACS Applied Materials & Interfaces 10 (14) (2018) 11979–11986. doi:10.1021/acsami.7b17488.
URL https://pubs.acs.org/doi/10.1021/acsami.7b17488

[32] S. Protiere, C. Duprat, H. A. Stone, Wetting on two parallel fibers: drop to column transitions, Soft Matter 9 (1) (2013) 271–276. doi:10.1039/C2SM27075G.
URL http://xlink.rsc.org/?DOI=C2SM27075G

[33] P. Wang, J. Zhou, B. Xu, C. Lu, Q. Meng, H. Liu, Bioinspired Anti-Plateau–Rayleigh-Instability on Dual Parallel Fibers, Advanced Materials 32 (45) (2020) 2003453. doi:10.1002/adma.202003453.
URL https://onlinelibrary.wiley.com/doi/10.1002/adma.202003453

[34] K. Steiros, M. Hultmark, Drag on flat plates of arbitrary porosity, Journal of Fluid Mechanics 853 (2018) R3. doi:10.1017/jfm.2018.621.
URL https://www.cambridge.org/core/product/identifier/S0022112018006213/type/journal_article

[35] G. I. Taylor, Air resistance of a flat plate of very porous material, Aeronautical Research Council, Reports and Memoranda 2236 (1944) 159–162.

[36] A. Roshko, On the wake and drag of bluff bodies, Journal of the aeronautical sciences 22 (2) (1955) 124–132.

[37] J.-K. Koo, D. F. James, Fluid flow around and through a screen, Journal of Fluid Mechanics 60 (3) (1973) 513–538.

[38] W. Shi, L. H. De Koninck, B. J. Hart, N. G. Kowalski, A. P. Fugaro, T. W. van der Sloot, R. S. Ott, B. S. Kennedy, J. B. Boreyko, Harps under Heavy Fog Conditions: Superior to Meshes but Prone to Tangling, ACS Applied Materials & Interfaces 12 (42) (2020) 48124–48132. doi:10.1021/acsami.0c12329.
URL https://pubs.acs.org/doi/10.1021/acsami.0c12329

[39] F. ECHEVARRIA JOHNSON, AERODYNAMIC AND GEOMETRIC CHARACTERIZATIONS FOR FOG COLLECTING MESHES, Ph.D. thesis, PONTIFICIA UNIVERSIDAD CATOLICA DE CHILE (2015).

[40] D. Degefie, T.-S. El-Madany, J. Hejkal, M. Held, J.-C. Dupont, M. Haeffelin, O. Klemm, Microphysics and energy and water fluxes of various fog types at sirta, france, Atmospheric Research 151 (2015) 162–175.

[41] J.-C. Dupont, M. Haeffelin, E. Wærsted, J. Delanoe, J.-B. Renard, J. Preissler, C. O'Dowd, Evaluation of Fog and Low Stratus Cloud Microphysical Properties Derived from In Situ Sensor, Cloud Radar and SYRSOC Algorithm, Atmosphere 9 (5) (2018) 169. doi:10.3390/atmos9050169.
URL http://www.mdpi.com/2073-4433/9/5/169

[42] M. Haeffelin, T. Bergot, T. Elias, R. Tardif, D. Carrer, P. Chazette, M. Colomb, P. Drobinski, E. Dupont, J.-C. Dupont, L. Gomes, L. Musson-Genon, C. Pietras, A. Plana-Fattori, A. Protat, J. Rangognio, J.-C. Raut, S. Rémy, D. Richard, J. Sciare, X. Zhang, Parisfog: Shedding new Light on Fog Physical Processes, Bulletin of the American Meteorological Society 91 (6) (2010) 767–783. doi:10.1175/2009BAMS2671.1.
URL https://journals.ametsoc.org/doi/10.1175/2009BAMS2671.1

[43] J. C. Dupont, M. Haeffelin, S. Stolaki, T. Elias, Analysis of Dynamical and Thermal Processes Driving Fog and Quasi-Fog Life Cycles Using the 2010–2013 ParisFog Dataset, Pure and Applied Geophysics 173 (4) (2016) 1337–1358. doi:10.1007/s00024-015-1159-x.
URL http://link.springer.com/10.1007/s00024-015-1159-x

[44] C. Duprat, S. Protiere, Capillary stretching of fibers, EPL (Europhysics Letters) 111 (5) (2015) 56006. doi:10.1209/0295-5075/111/56006.
URL https://iopscience.iop.org/article/10.1209/0295-5075/111/56006

[45] A. Rewakowicz, J. M. Chomaz, C. Duprat, Mist collector: Art and science project, in: 7th International Conference on Fog, Fog Collection and Dew, 2016.